Preprint
UCRL-JC-149147

4.5-and 8-keV Emission and Absorption X-ray Imaging Using Spherically Bent Quartz 203 and 211 Crystals

J. A. Koch, Y. Aglitskiy, J. Seely, C. Brown, G. Holland

This article was submitted to
14th Topical Conference on High Temperature Plasma Diagnostics,
Madison, WI., July 8-11, 2002

July 12, 2002

This work was performed under the auspices of the United States Department of Energy by the University of California, Lawrence Livermore National Laboratory under contract No. W-7405-Eng-48.

4.5- and 8-keV Emission and Absorption X-ray Imaging Using Spherically Bent Quartz 203 and 211 Crystals

J. A. Koch[a], Y. Aglitskiy[b], J. Seely[c], C. Brown[c], G. Holland[c]

[a] *University of California, Lawrence Livermore National Laboratory, Livermore CA, 94551*
[b] *Science Applications International Corporation, McLean VA, 22102*
[c] *Naval Research Laboratory, Washington DC, 20375*

Abstract

We have used spherically-bent quartz 203 and 211 crystals to image 4.5- and 8-keV sources in both emission and absorption geometries. These imaging systems are straightforward to align, provide high throughput, and can provide high spatial resolution over large fields-of-view. We discuss the imaging geometry and alignment strategies, and we present experimental results we have obtained from 1 ns-duration multi-kilojoule laser facilities and from sub-ps-duration ultra-high-intensity laser facilities. Our successful applications suggest that high-quality spherically-bent quartz crystals may be used to image at many different x-ray energies due to the numerous diffraction planes available from quartz. This range of usable x-ray energies increases the number of applications that might benefit from high-resolution, high-brightness monochromatic x-ray imaging using bent crystals.

I. Introduction

Two-dimensionally bent Bragg imaging crystals are becoming routine tools for multi-keV x-ray imaging of plasmas [1-13]. The imaging properties of spherically-bent crystals, analogous to spherical mirrors, can be understood on the basis of simple geometrical optics, and they can provide high spatial resolution over large fields-of-view provided the angle of incidence is within several degrees of normal; this is necessary in order to minimize astigmatism. The restriction on the angle of incidence θ, along with the fixed interplanar spacing (d) of the crystal itself, restricts the operating wavelength (λ) for a particular crystal to a narrow range to the short-wavelength side of $\lambda = 2d$; this is because the Bragg equation $\lambda = 2d\sin\theta$ must be satisfied. Very high-quality convex spherical mandrels can be used to produce excellent concave-spherical surface figures on bent crystals using optical-contact fabrication techniques [1], allowing high-quality x-ray images to be obtained when the crystal structure itself is nearly perfect. X-ray images have been obtained using Bragg reflections of various bent crystals, including quartz 100 [1], quartz 101 [3 - 5], mica [6 - 8], thallium acid phthalate [9], Si 311 [10, 11], and Ge 311 [10, 11]. Quartz 101 has been shown to allow ~ 2 μm-resolution imaging at 1.8 keV [3].

The principle restriction on the utility of spherically-bent crystals is the geometrical-optics-based requirement that the angle of incidence must be very close to normal. This restriction, coupled with the limited number of suitably-high-quality x-ray crystals and their fixed interplanar spacings, leads to a limited number of suitable x-ray imaging wavelengths. One approach to broadening the range of suitable imaging wavelengths is to use toroidally-bent crystals, which use different sagittal and meridional radii of curvature to eliminate astigmatism for incident angles far from normal [1, 9-11]. However, high-quality toroidal surfaces are much more complex to fabricate, and the

resulting imaging optic is difficult to align due to constraints on all 6 degrees of positioning freedom. A second approach to broadening the range of suitable imaging wavelengths is to broaden the range of suitably-high-quality x-ray crystals, by developing the capability to manufacture and bend different crystals and crystal cuts [2]. This second approach has provided the motivation for the present work.

Due to the structural properties of framework silicates, quartz crystals contain numerous planes with different interplanar spacings which are suitable for Bragg diffraction. Quartz is also a high-quality naturally-occurring crystal which has been used extensively for x-ray imaging. Previous work [2] suggested several other planes of quartz which might be suitable for x-ray imaging, including 203 (2d = 2.749 Å) and 211 (2d = 3.082 Å). In this paper, we describe experimental results we have obtained utilizing spherically-bent quartz 203 and 211 crystals to image at 4.5 and 8 keV. These results demonstrate the general utility of quartz as an x-ray imaging crystal at a variety of wavelengths, using various cuts and diffraction orders, and demonstrate how these imaging crystals can be simply positioned and aligned for application to laser-produced plasma experiments.

II. Spherical Crystal Fabrication and Testing

We used three different quartz crystals for our experiments. The first quartz 203 crystal was obtained from Crismatec [14], and was 40 mm in diameter with a 356-mm radius of curvature. The second quartz 203 crystal and the quartz 211 crystal were obtained from Extar [15], and were 35 mm in diameter with 380-mm radii of curvature. The Extar crystals were fabricated by optical contact techniques [1], and proved to be of superior quality compared with the Crismatec crystal.

Tests were performed on both quartz 203 crystals with a Manson-type x-ray source emitting 4.5 keV Ti K-α x-rays. In the first of these tests (using the Crismatec crystal), the x-ray source was placed on the Rowland circle at an object distance $p_s = R$, where R is the crystal radius (see Fig. 1). The source back-illuminated a grid at an object distance p, and the grid was imaged by the crystal onto Kodak DEF (direct exposure x-ray film) at an image distance $q = pR/(2p-R)$. Astigmatism results in different meridional and sagittal focus planes q_m and q_s, with $q_m = pR\sin\theta/(2p-R\sin\theta)$ and $q_s = pR/(2p\sin\theta-R)$, where θ is the Bragg angle measured from the crystal surface. We place the film plane at $q = pR/(2p-R)$, approximately midway between q_m and q_s, so as to produce a round point-spread function [2].

In this geometry, the local spatial resolution at the object plane is determined first by the source size and the Bragg angle (due to astigmatism), and second by the local crystal quality. The latter consideration results because each point at the object is imaged by a small region of the crystal, with the size of the crystal determining the field of view rather than the spatial resolution. The x-ray source size was restricted so as to have minimal impact on the spatial resolution obtained in the images, and the images therefore provide a map of local crystal quality. This Rowland-circle backlight geometry (Fig. 2(a)) contrasts with the emitting-object and area-backlight geometries (Fig. 2(b)), where the spatial resolution is determined first by the area of the crystal and the Bragg angle, and second by the crystal quality averaged over the full aperture of the crystal.

The Crismatec crystal was tested with a grid consisting of 6 μm Au wires on a 25.4-μm period. The grid was imaged by the crystal at 7X-magnification, producing the map shown in Fig. 3. The overall quality of the crystal is good, and in localized regions it achieves spatial resolutions better

than 7 μm, assuming that simple quadrature addition of the wire width and the line-spread function width determines the final image width. However, different regions of the crystal appear to suffer from localized deformations that result in poor focusing, and this limits the useful aperture of the crystal. This, in turn, limits either the field of view obtainable with the crystal in the Rowland-circle backlight geometry, or limits the light-collection numerical aperture in emitting-object or area-backlight geometries.

For testing the Extar quartz 203 crystal, we used the area backlight geometry of Fig. 2(b). In these tests, the x-ray source was moved close to the grid, so that each point on the grid was imaged by a region of the crystal that was approximately 7 mm across. For these tests, we used a grid consisting of 8 μm Au wires on a 62.5-μm period. The grid was imaged by the crystal at 7X-magnification, producing the map shown in Fig. 4. The quality of the crystal is excellent, and spatial resolutions better than 8 μm were obtained despite the large averaging surface area of the crystal.

III. Backlit Imaging Experiment

Our backlit imaging experiment was performed on the Nova Laser Facility at Lawrence Livermore National Laboratory, and utilized a laser-irradiated scandium foil as an x-ray source to backlight a gold grid in the area-backlight geometry of Fig. 2(b). The geometry of this experiment is shown in Fig. 5. Two beams of the Nova laser delivered a total of 3.6 kJ of 0.351-μm laser light in a 1-ns pulse onto the central ~ 700 μm of the front surface of a 2 mm square, 25 μm-thick Sc foil placed 5.1 mm behind a 63.5 μm-period Au grid. The Crismatec quartz 203 crystal was used to image the Au grid onto a gated microchannel-plate intensified framing camera [16] at a magnification of M = 17. The magnified image overlapped two separately-timed strips of the

4-strip camera, which was configured to provide 0.5-ns inter-strip time delays. The crystal was approximately 190 mm from the grid, and the image plane was approximately 3 meters from the grid on the opposite side of the target chamber.

The backlight foil produced line emission from highly-ionized Sc, and we tuned the crystal to image in the light of Sc Ly-α at 2.736 Å by using a first-order Bragg angle of 84.43° [17]. The crystal was apertured to D = 2 mm using an Al shield, providing a predicted astigmatism-limited object spatial resolution $\sigma = (M+1)(1-\sin\theta)D/M$ of 10 μm [2]. The framing camera was shielded by a 25 μm-thick Ta foil from a direct view of the backlight foil, and all target components (the grid, shielding foil and backlight foil) were mounted onto a cylindrical Au hohlraum of the type used for indirect-drive inertial-confinement fusion (ICF) experiments [18] (Fig. 5). This target packaging was utilized in order to allow standard ICF target fabrication and target alignment procedures to be used; no laser beams irradiated the hohlraum.

The crystal was positioned at the end of a manipulator arm that provided three degrees of alignment freedom; tip, tilt, and axial position. The tip and tilt motions were pivoted approximately 2.5 meters away from the target, behind the crystal, and for practical purposes these motions become lateral x and y. The crystal was housed on a goniometer stage with an angular adjustment that was used to set the Bragg angle.

Alignment was accomplished using the following method. First, a rigid mechanical pointer was bench-aligned to the crystal housing and served to locate the center of the crystal at the proper spherical coordinates relative to the grid location and the axis of the manipulator arm. A pencil-beam laser, projecting from the detector location, was then pointed at the crystal, and the

crystal was adjusted using the goniometer stage and lateral x and y until the reflection of the pencil laser beam returned to the detector. This procedure set the zero angle for later Bragg angle adjustments, and defined the axis from the detector to the center of the crystal.

The Bragg angle was then set using a pre-calculated angular offset, and a second, line-projection laser was used to verify that the correct Bragg geometry had been obtained. This laser reflected off an annular mirror that had been prealigned to the proper angle with respect to the crystal axis, and back-reflected to the detector location when the proper Bragg angle had been achieved. The focus of the pencil-beam laser was observed at the location of the object with high-magnification cameras, and fine-tuning of the crystal location and angle was performed until the focus was at the desired location with the correct Bragg angle. Finally, the known angular offset between the crystal planes and the crystal surface was corrected by a final angular adjustment that was verified by the line-projection laser beam reflection moving by a pre-calculated amount at the detector location.

We note that this alignment procedure relies upon knowledge of the target chamber layout (e.g. from mechanical drawings), requires that the crystal radius be known in advance, and requires that any angular offset between the crystal surface and the x-ray diffracting planes be known in advance. No final check was made to verify that optimum imaging conditions had been obtained, and while this proved adequate for these experiments, we did make such a check in later experiments described in Section IV.

The data we obtained in this experiment is shown in Figure 6. Signal-to-noise for this experiment was poor because of the very low brightness of the Sc Ly-α emission line [19]. Nevertheless, the spatial resolution we

obtained was in good agreement with pre-shot predictions based on the Bragg angle and the crystal aperture, and the image brightness we obtained was within a factor of ~ 3 of pre-shot predictions. Experience from this experiment allowed us to improve the imaging system for subsequent experiments described in the next section, and the experiment demonstrated that crystal imaging was feasible using opposed manipulator arms to hold the crystal and the detector.

IV. Emission Imaging

Our emission imaging experiments were performed at the Laboratoire pour l'Utilisation des Lasers Intenses (LULI) at Ecole Polytechnique, France, and at the Rutherford Appleton Laboratory (RAL) laser facility, United Kingdom. In these experiments we irradiated sandwich targets, consisting of a Ti or Cu tracer layer embedded within solid aluminum or plastic, with ultra-high-intensity laser light. Laser-plasma interactions produce strong currents of relativistic electrons which propagate through the target and excite K-α fluorescence within the tracer layer, and this K-α fluorescence was used as a diagnostic of relativistic electron transport within the target [20, 21]. The physical results from these experiments will be published elsewhere, and we concentrate here on the diagnostic configuration.

In the LULI experiments, we irradiated the targets with 20 J, 1.054-μm, 0.4 ps laser light focused to peak intensities in excess of 10^{19} W/cm^2. The laser was focused onto the front surface of the target, and we used the Extar quartz 203 crystal to image Ti K-α emission from buried Ti tracer layers onto a charge-coupled device (CCD) detector at a magnification of M = 8 (Fig. 7). As in the backlit-imaging experiments described in Section III, we placed the camera at a distance q = pR/(2p-R) in order to produce a round point-spread

function. The first-order Bragg angle for Ti K-α is 88.9 degrees, but we used a central Bragg angle of 88.1 degrees in order to increase the spectral range contained within the image and to provide greater tolerance for alignment errors. We utilized a 16 mm-diameter aperture at the crystal, and this provided a predicted astigmatism-limited object spatial resolution $\sigma = (M+1)(1-\sin\theta)D/M$ of 10 μm [2]. The detector pixels were 25 μm-square in a 1024x1024 array, providing a ~ 25 mm field of view at the target with a pixel-limited object spatial resolution of ~ 3 μm. The pixel-limited object resolution is much less than the astigmatism-limited object resolution of ~ 10 μm, indicating that the detector oversamples the object and that the primary limitation to object resolution is the crystal itself.

In order to align the imager for these experiments, we first positioned the crystal at approximately the correct distance from the target, behind the target along the detector/target axis. We used a pencil laser beam (incident through a glass port at the detector position) to illuminate a marker placed at the intended object location (defined by fixed viewing cameras), and manipulated the crystal in x/y/tip/tilt until the back-reflection returned through the glass port.

We next placed a laser light-emitting single-mode optical fiber at the intended object position, with the diverging beam pointed roughly at the expected final crystal position, and we replaced the glass port at the detector with the CCD camera. We then made a pre-calculated angular offset of the crystal in the horizontal plane to account for the desired Bragg angle, and we moved the crystal within the horizontal plane using x/y/z motion only until the best-focus image of the point source fell at the center of the CCD camera. We then installed Be and Ti x-ray filters in front of the CCD camera, and we inserted a Be blast shield in front of the crystal to protect it from target debris.

Like the procedure described in Section III, this alignment procedure relies upon knowledge of the target chamber layout (e.g. from mechanical drawings), and requires that the crystal radius be known in advance. Unlike the procedure described in Section III, this procedure does provide a final verification that best focus has been achieved. We note that we did not make a pre-calculated angular adjustment to compensate for the angular offset between the crystal surface and the x-ray diffraction planes, since in these experiments the angular offset was small enough that the x-ray spot fell on the CCD chip when the optical spot was centered. Once the x-ray spot was observed, it was adjusted to be at the center of the CCD chip using tip/tilt angular adjustments alone.

In the RAL experiments, we irradiated the targets with 100 J, 0.527-μm, 1 ps laser light focused to intensities in excess of 10^{19} W/cm^2, and used the Extar quartz 211 crystal to image Cu K-α emission onto a thinned, back-illuminated charge-coupled device (CCD) detector at a magnification of M = 8 using the second Bragg diffraction order. The configuration of these experiments, and the alignment strategy, was identical to the LULI experiments described above. The Bragg angle in this case was also 88.1 degrees, and we again utilized a 16 mm-diameter aperture at the crystal. The predicted astigmatism-limited object spatial resolution was again σ = 10 μm, and the same CCD camera was used in both the RAL experiments and the LULI experiments.

Typical data from these experiments is shown in Figure 8. The crystal imager worked well with both Ti and Cu tracer layers, providing well-exposed images onto the CCD. Peak signal levels were 3 - 10 times the background noise level due to a variety of sources, including fluorescence from the chamber walls and high-energy x-rays penetrating the shielding between the

detector and the target. The Ti image brightness was roughly in agreement with pre-shot analytical predictions [2], but the Cu images from RAL were in fact brighter than the Ti images from LULI, in disagreement with pre-shot calculations that predicted the image brightness would be weaker despite the increase in on-target laser energy from 20 J to 100 J. This fortunate result was unexpected, but we are unaware of any experimental measurements of the integrated reflectivity of either quartz 203 or quartz 211, and so we were forced to use calculated flat-crystal values derived from an idealized Darwin-Prins model [22]. While this model apparently works reasonably well for quartz 203 at 4.5 keV, it is inadequate for quartz 211 at 8 keV. The x-ray image data obtained from the LULI and RAL experiments have provided a wealth of information about electron transport in solid targets that is currently being analyzed, and the results will be published elsewhere.

V. Summary and Conclusions

In summary, we have demonstrated that quartz is a good choice for use in spherically-bent crystal imagers at a variety of x-ray energies, in the first or the second Bragg diffraction order, due to the numerous diffraction planes available in quartz and due to the high perfection obtainable from carefully selected quartz crystals. We have described alignment procedures that are sufficiently precise and reproducible to allow sub-10-μm object resolution to be obtained routinely, with higher resolution clearly achievable from sufficiently high-quality crystals with surface areas small enough to minimize the effects of crystal imperfections and astigmatism [3]. We have performed several experiments using spherically-bent quartz 203 and quartz 211 crystals to obtain quasi-monochromatic x-ray images at 4.5 and 8 keV, in a 1 ns-duration multi-kilojoule laser facility and in two sub-ps-duration ultra-high-

intensity laser facilities. The data are of high quality when the source is sufficiently bright, and the ultra-high-intensity laser data have provided a wealth of information about electron transport in solid targets that cannot be obtained through other techniques.

We acknowledge the collaborative efforts of F. Amiranoff, C. Andersen, T. Barbee Jr., D. Batani, S. D. Baton, T. E. Cowan, N. Fisch, R. R. Freeman, L. Gremillet, T. A. Hall, S. J. Hatchett, J. M. Hill, M. H. Key, J. King, M. Koenig, B. F. Lasinski, A. B. Langdon, A. J. MacKinnon, E. Martinolli, P. Norreys, P. Parks, E. Perelli-Cippo, M. Rabec Le Gloahec, M. Rosenbluth, C. Rousseaux, J. J. Santos, F. Scianitti, R. A. Snavely, and R.B. Stephens in planning, executing and analyzing the LULI and RAL experiments, and we acknowledge the efforts of A. Faenov and T. Pikuz in manufacturing the Extar crystals that were successfully used in these experiments. This work was performed under the auspices of the U.S. Department of Energy by the University of California Lawrence Livermore National Laboratory under contract No. W-7405-ENG-48.

References

[1] E. Förster, K. Gabel, I. Uschmann, Laser and Particle Beams **9**, 135 (1991).

[2] J. A. Koch, O. L. Landen, T. W. Barbee, Jr., P. Celliers, L. B. Da Silva, S. G. Glendinning, B. A. Hammel, D. H. Kalantar, C. Brown, J. Seely, G. R. Bennett, W. Hsing, Appl. Opt. **37**, 1784 (1998).

[3] Y. Aglitskiy, T. Lehecka, S. Obenschain, S. Bodner, C. Pawley, K. Gerber, J. Sethian, C. M. Brown, J. Seely, U. Feldman, G. Holland, Appl. Opt. **37**, 5253 (1998).

[4] Y. Aglitskiy, A. L. Velikovich, M. Karasik, V. Serlin, C. J. Pawley, A. J. Schmitt, S. P. Obenschain, A. N. Mostovych, J. H. Gardner, N. Metzler, Phys. Rev. Lett. **87**, 265001 (2001).

[5] Y. Aglitskiy, A. L. Velikovich, M. Karasik, V. Serlin, C. J. Pawley, A. J. Schmitt, S. P. Obenschain, A. N. Mostovych, J. H. Gardner, N. Metzler, Phys. Rev. Lett. **87**, 265002 (2001).

[6] T. A. Pikuz, A. Y. Faenov, M. Fraenkel, A. Zigler, F. Flora, S. Bollanti, P. Di Lazzaro, T. Letardi, A. Grilli, L. Palladino, G. Tomassetti, A. Reale, L. Reale, A. Scafati, T. Limongi, F. Bonfigli, L. Alainelli, M. S. Del Rio, Laser and Particle Beams **19**, 285 (2001).

[7] F. Blasco, C. Stenz, F. Salin, A. Y. Faenov, A. I. Magunov, T. A. Pikuz, I. Y. Skobelev, Rev. Sci. Instruments **72**, 1956 (2001).

[8] S. Pikuz, T. Shelkovenko, V. Romanova, D. Hammer, A. Faenov, V. Dyakin, T. Pikuz, Rev. Sci. Instruments **68**, 740 (1997).

[9] M. Vollbrecht, O. Treichel, I. Uschmann, K. Gäbel, R. Lebert, E. Förster, Appl. Opt. **37**, 1803 (1998).

[10] I. Uschmann, E. Förster, H. Nishimura, K. Fujita, Y. Kato, S. Nakai, Rev. Sci. Instruments **66**, 734 (1995).

[11] I. Uschmann, K. Fujita, I. Niki, R. Butzbach, H. Nishimura, J. Funakura, M. Nakai, E. Förster, K. Mima, Appl. Opt. **39**, 5865 (2000).

[12] Y. Ochi, K. Fujita, I. Niki, H. Nishimura, N. Izumi, A. Sunahara, S. Naruo, T. Kawamura, M. Fukao, H. Shiraga, H. Takabe, K. Mima, S. Nakai, I. Uschmann, R. Butzbach, E. Forster, J. Quant. Spectroscopy and Rad. Transfer **65**, 393 (2000).

[13] I. Uschmann, P. Gibbon, D. Klopfel, T. Feurer, E. Förster, P. Audebert, J. P. Geindre, J. C. Gauthier, A. Rousse, C. Rischel, Laser and Particle Beams **17**, 671 (1999).

[14] Crismatec, Saint-Pierre-lès-Nemours, France.

[15] Extar International, Ltd., Sheridan, Oregon, U.S.A.

[16] J. D. Kilkenny, Laser and Particle Beams **9**, 49 (1991).

[17] J. A. Koch, O. L. Landen, T. Barbee, Jr., G. Bennett, C. Brown, P. Celliers, G. Collins, L. Da Silva, S. Glendinning, S. Haan, B. Hammel, W. Hsing, D. Kalantar, M. Key, J. Seely, L. Suter, F. Weber, Rev. Sci. Instrum. **70**, 525 (1999).

[18] J. Lindl, Plasma Physics **2**, 3933 (1995).

[19] The Sc Ly-α line is typically a factor of 15 less intense than the He-α line in these experiments; see S. G. Glendinning *et al.*, Phys. Plasmas **7**, 2033 (2000).

[20] J. A. Koch, M. H. Key, R. R. Freeman, S. P. Hatchett, R. W. Lee, D. Pennington, R. B. Stephens, M. Tabak, Phys. Rev. E **65**, 106410 (2001).

[21] M. H. Key, Y. Aglitskiy, F. Amiranoff, C. Andersen, D. Batani, S. Baton, T. E. Cowan, N. Fisch, R. R. Freeman, L. Gremillet, T. A. Hall, S. J. Hatchett, J. M. Hill, J. King, J. A. Koch, M. Koenig, B. F. Lasinski, A. B. Langdon, A. J. MacKinnon, E. Martinolli, P. Norreys, P. B. Parks, E. Perelli-Cippo, M. Rabec Le Gloahec, M. N. Rosenbluth, C. Rousseaux, J. J. Santos, F. Scianitti,

R. A. Snavely, R. B. Stephens, Proceedings of the Inertial Fusion Sciences and Applications Conference, 2001 (in press).

[22] B. L. Henke, E. M. Gullikson, J. C. Davis, Atomic Data and Nuclear Data Tables **54**, 2 (1993).

Figure Captions

Figure 1. Geometry of the point-backlight tests. An x-ray source back-illuminated the grid, which was imaged by the crystal onto Kodak direct-exposure x-ray film. The film plane was placed between the meridional and sagittal foci in order to obtain a round point-spread function. In the area-backlight tests, the x-ray source was moved inside the Rowland circle to just behind the grid.

Figure 2. Comparison between the point-backlight geometry (a) and the area-backlight/emission geometry (b). In (a), the local spatial resolution at the object plane is determined first by the source size and the Bragg angle (due to astigmatism) and second by the local crystal quality, and the field of view is determined by the crystal aperture. In (b), the spatial resolution is determined first by the area of the crystal and the Bragg angle and second by the crystal quality averaged over the full aperture of the crystal, and the field of view is determined by the backlight area (or is unlimited in the case of emission imaging).

Figure 3. Point-backlit test image of a Au grid with 25.4 μm period and 6 μm wires, obtained at 4.5 keV using the Crismatec quartz 203 crystal. Localized regions of the crystal are of sufficient quality to produce 9 μm FWHM (full width at half maximum intensity) images of the 6 μm wires, implying that the FWHM of the point-spread function is better than 7 μm. The images and lineouts are in scaled units of film optical density, and have not been converted to exposure.

Figure 4. Area-backlit test image of a Au grid with 62.5 μm period and 8 μm wires, obtained at 4.5 keV using the Extar quartz 203 crystal. The area of the crystal used to obtain this image was approximately 7 mm across, and this region produced 11 μm FWHM (full width at half maximum intensity) images of the 8 μm wires, implying that the FWHM of the point-spread function is better than 8 μm. The images and lineouts are in scaled units of film optical density, and have not been converted to exposure.

Figure 5. Geometry of the Nova Sc Ly-α backlight experiment. The Sc foil back-illuminated a grid in the area backlight geometry of Fig. 2(b), and the grid was imaged onto a microchannel-plate intensified gated framing camera on the opposite side of the target chamber.

Figure 6. Data from the Nova Sc Ly-α backlight experiment, obtained from one strip of the microchannel-plate intensified gated framing camera. Low signal-to-noise (approximately 1.5) resulted from the very weak emission of the 4.53 keV Sc Ly-α line. The broad light horizontal band towards the bottom of the image is an artifact of the framing camera. Spatial resolution is estimated to be approximately 10 μm at the object.

Figure 7. Geometry of the LULI and RAL Ti K-α and Cu K-α emission imaging experiments. The direct line of sight from the target to the CCD detector was blocked by a thick Ta shield.

Figure 8. Typical data from the Ti K-α experiments at LULI (a) and from the Cu K-α experiments at RAL (b). The spatial scales are approximately 200 μm across the images, and the small spot in (a) is 4.5 keV bremsstrahlung emitted

from the laser/target interaction plasma on the front surface of the target, viewed through the Ti tracer layer. The front surface plasma is offset from the K-a image because the crystal viewed the rear surface from approximately 45° off the surface normal.

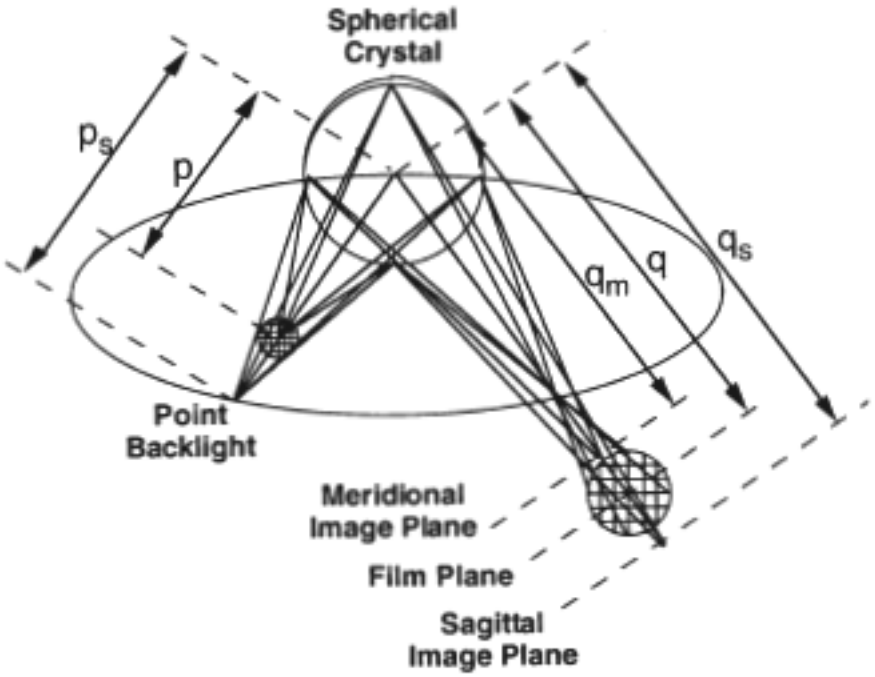

Figure 1, J. A. Koch et al., RSI

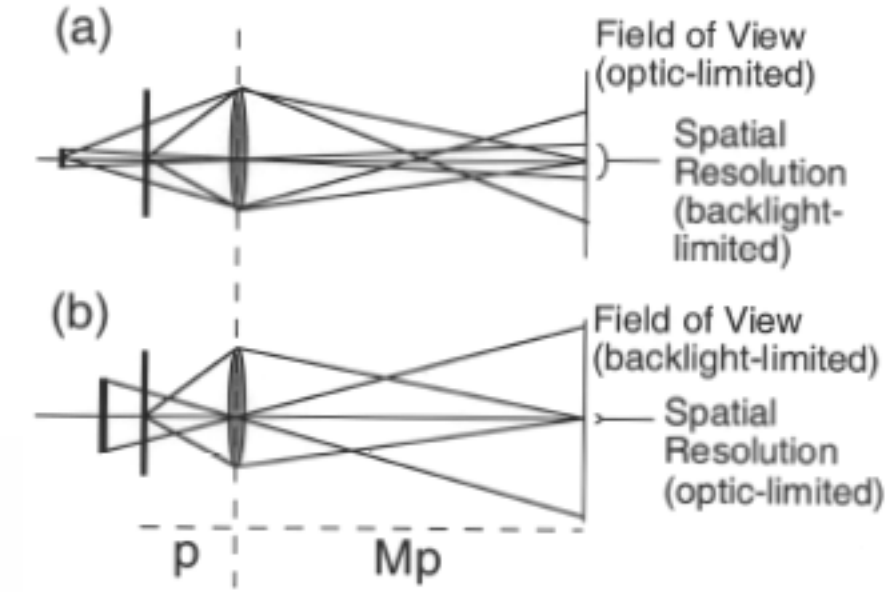

Figure 2, J. A. Koch et al., RSI

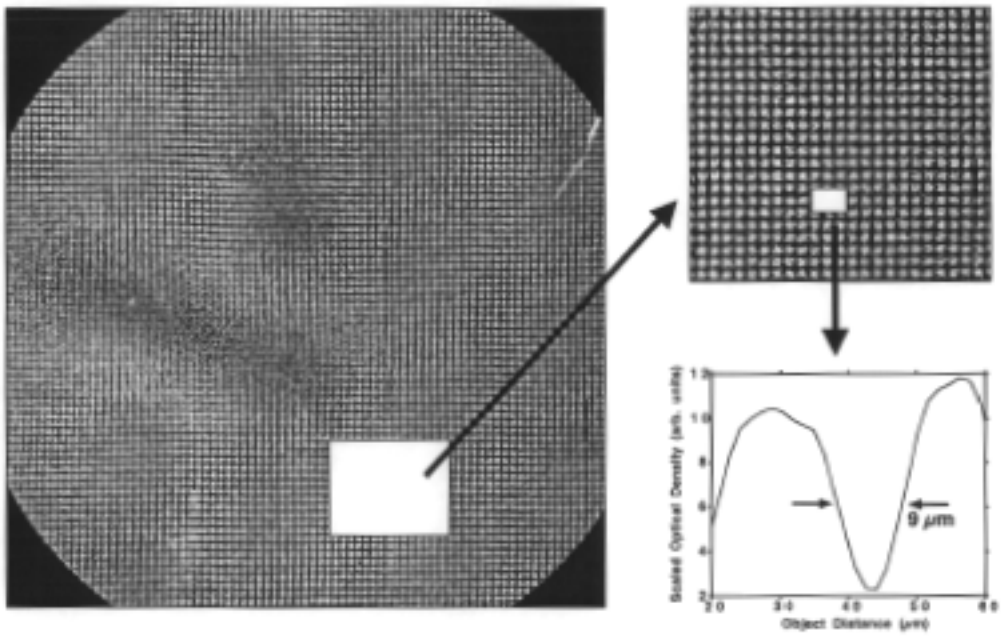

Figure 3, J. A. Koch et al., RSI

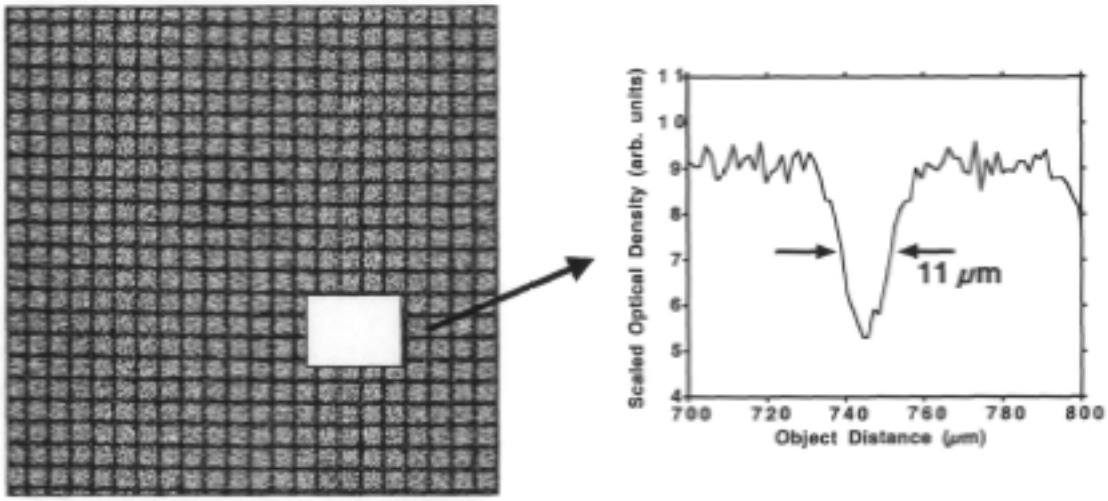

Figure 4, J. A. Koch et al., RSI

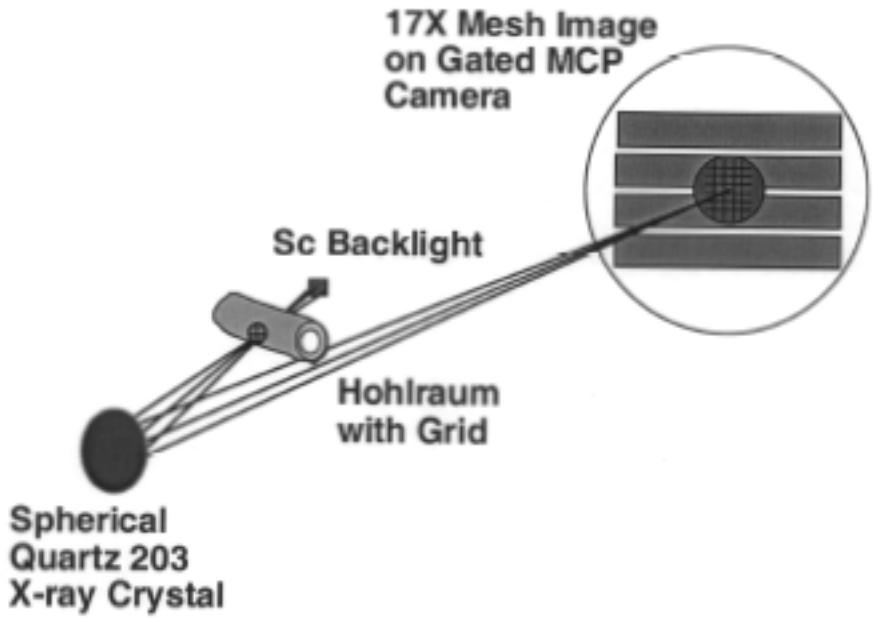

Figure 5, J. A. Koch et al., RSI

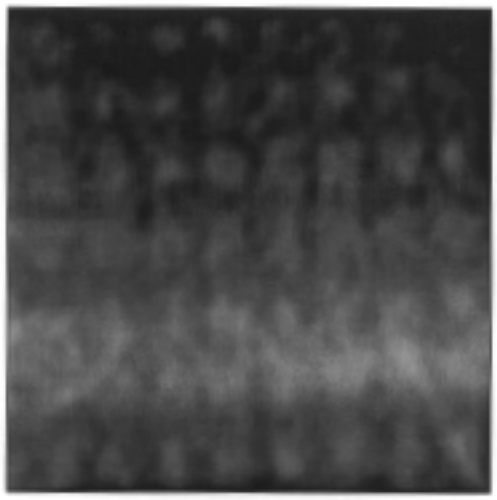

Figure 6, J. A. Koch et al., RSI

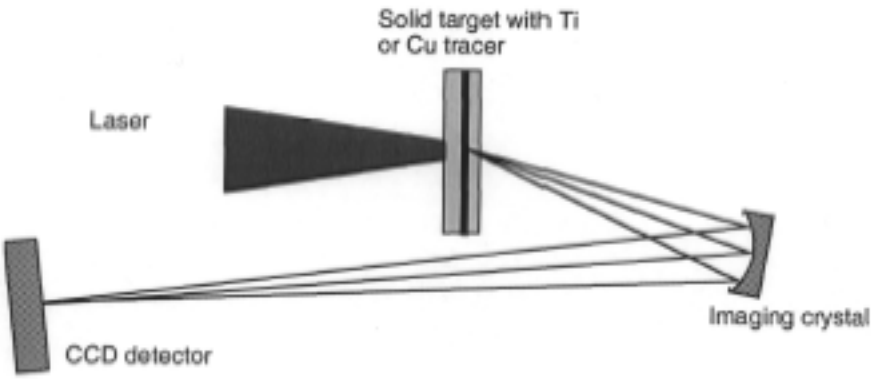

Figure 7, J. A. Koch et al., RSI

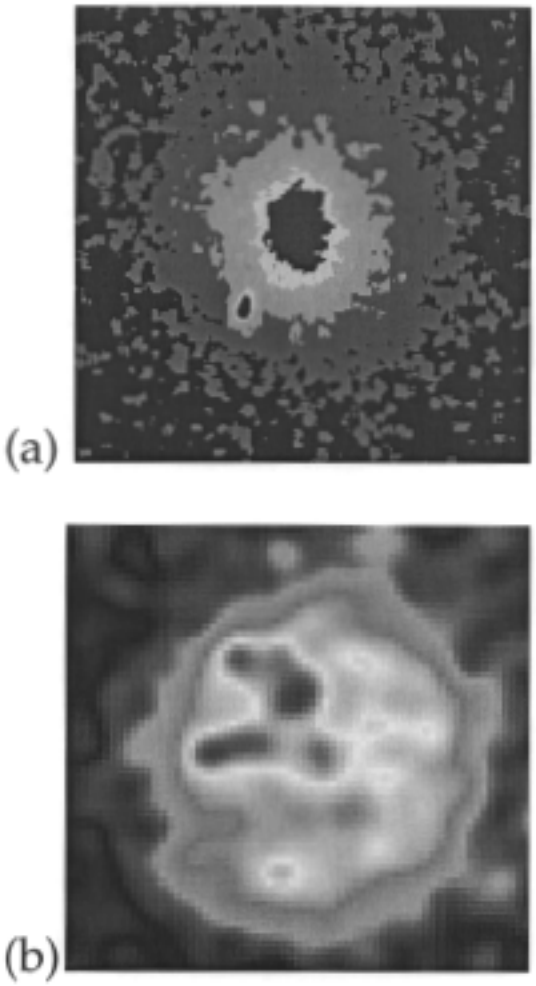

Figure 7, J. A. Koch et al., RSI